

Mixing state and effective density of aerosol particles during the Beijing 2022 Olympic Winter Games

Aodong Du^{1,2}, Jiaxing Sun^{1,2}, Hang Liu¹, Weiqi Xu¹, Wei Zhou¹, Yuting Zhang^{1,2}, Lei Li³, Xubing Du^{3,4}, Yan Li^{1,2}, Xiaole Pan¹, Zifa Wang^{1,2}, and Yele Sun^{1,2}

5 ¹State Key Laboratory of Atmospheric Boundary Layer Physics and Atmospheric Chemistry, Institute of Atmospheric Physics, Chinese Academy of Sciences, Beijing 100029, China

²College of Earth and Planetary Sciences, University of Chinese Academy of Sciences, Beijing 100049, China

³Institute of Mass Spectrometry and Atmospheric Environment, Jinan University, Guangzhou 510632, China

⁴Guangdong Provincial Engineering Research Center for On-Line Source Apportionment System of Air Pollution, 10 Guangzhou 510632, China

Correspondence to: Yele Sun (sunyele@mail.iap.ac.cn)

Abstract. Mixing state and density are two key parameters of aerosol particles affecting their impacts on radiative forcing and human health. Here a single particle aerosol mass spectrometer in tandem with a differential mobility analyzer and an aerodynamic aerosol classifier was deployed during the Beijing 2022 Olympic Winter Games (OWG) to investigate the impacts of emission controls on particle mixing state and density. Nearly 760,000 particles were detected, which were classified into seven major classes. Our results show the dominance of carbonaceous particles comprising mainly Total-Elemental Carbon (Total-EC, 13.4 %), Total-Organic Carbon (Total-OC, 10.5 %) and Total-ECOC (47.1 %). Particularly, the particles containing organic carbon and sulfate were enhanced significantly during OWG although those from primary emissions decreased. The composition of carbonaceous particles also changed significantly which was characterized by the decreases in EC-Nitrate and Sulfate (EC-NS), EC-Potassium Nitrate (KEC-N), and amine-containing particles, and increase in ECOC-Nitrate and Sulfate (ECOC-NS). This result indicates that emission controls during OWG reduced the mixing of EC with inorganic aerosol species and amines, yet increased the mixing of EC with organic aerosol. The average effective density (ρ_{eff}) of aerosol particles (150–300 nm) was 1.15 g cm⁻³ during the non-Olympic Winter Games (nOWG), with higher values during OWG (1.26 g cm⁻³) due to the increase in secondary particle contribution. The two types of fresh particles, i.e., Total-EC and high molecular weight organic matter presented the lowest ρ_{eff} (0.97 g cm⁻³ and 0.87 g cm⁻³, respectively). In addition, the ρ_{eff} of most particles increased as the increases in pollution levels and relative humidity, yet varied differently for different types of particles, highlighting the impacts of aging and formation processes on the changes of particle density and mixing state.

1 Introduction

30 Atmospheric aerosols from both natural and anthropogenic sources exert strong influences on radiative forcing and human health (Buseck and Posfai, 1999; Anderson et al., 2003; Ramanathan et al., 2001; Prather, 2009; Charron et al., 2007), and the impacts depend strongly on their chemical and physical properties, e.g., composition, mixing state, and density. Beijing,

experiencing severe pollution with high concentrations of fine particulate matter over the past decade (Huang et al., 2014; Guo et al., 2014; Sun et al., 2016), has a great success in air pollution control (Lei et al., 2021a; Cheng et al., 2019), and the 35 annual average concentration of PM_{2.5} reached the Chinese National Ambient Air Quality Standard for the first time in 2021 (33 $\mu\text{g m}^{-3}$). However, polluted events still occurred occasionally, particularly during wintertime with stagnant meteorological conditions and high anthropogenic emissions (Lei et al., 2021b; Xu et al., 2022; Feng et al., 2022; Zhou et al., 2023). Short-term emission controls can improve air quality by reducing anthropogenic emissions temporarily, for example, the Beijing 40 2008 Summer Olympics (Wang et al., 2010; Okuda et al., 2011; Zhou et al., 2010), the 2014 Asia-Pacific Economic Cooperation (APEC) summit (Han et al., 2015; Gao et al., 2017; Ren et al., 2018), and the 2020 lockdown due to the corona virus disease (COVID-19) (Sun et al., 2020; Chang et al., 2022; Rajesh and Ramachandran, 2022; Zhang et al., 2022a). Similarly, the Chinese government imposed strict emission controls in Beijing and surrounding regions during the Olympic 45 Winter Games (OWG) in Beijing in 2022. These measures included shutting down factories with high emissions, limiting the number of vehicles, stopping construction activities, and forbidding fireworks, etc. (The People's Government of Beijing Municipality, 2022). As a result, the PM_{2.5} decreased significantly during OWG (Liu et al., 2022). Although the effects of emission controls on chemical composition and formation mechanisms of fine particles have been extensively studied, their impacts on chemical and physical properties of single particles, e.g., mixing state and effective density (ρ_{eff}) are poorly understood.

Single particle aerosol mass spectrometers (SPAMS) have been widely used to characterize mixing state, chemical 50 compositions and formation mechanisms of aerosol particles (Bhave et al., 2002; Giorio et al., 2015; Li et al., 2014; Bi et al., 2011; Chen et al., 2017; Zhang et al., 2018). Previous single particle studies in China were mainly conducted in polluted winters. Chen et al. (2020) found that carbonaceous particles associated with coal combustion were the main contributors of fine particles during wintertime in urban and rural areas of Beijing. Zhang et al. (2022b) found that the proportion of elemental 55 carbon particles mixed with organics gradually increased in winter from 2016 to 2019 in Chengdu. Similarly, elemental carbon particles tended to be more mixed with organics in winter in Beijing compared to summer (Xie et al., 2020). However, the measurements of critical parameters of aerosol particles, e.g., effective density (ρ_{eff}) with different mixing state, are still limited (Buseck and Posfai, 1999; Pitz et al., 2003).

ρ_{eff} reflecting the average density and morphological characteristics of particles depends strongly on mixing state, sources and aging levels (Decarlo et al., 2004). To obtain ρ_{eff} , SPAMS is often deployed along with other instruments that can measure 60 particle sizes as well. Spencer et al. (2007) deployed a differential mobility analyzer (DMA) and a SPAMS simultaneously, and determined the ρ_{eff} of aerosol particles in the range of ~1 to 1.5 g cm⁻³ in California in summer. Using the same system, Zhai et al. (2017) found that the ρ_{eff} of biomass combustion particles ranged from ~1.16 to 1.51 g cm⁻³. Recently, an aerodynamic aerosol classifier (AAC) tandem SPAMS system was established by Peng et al. (2021) to determine the volume 65 equivalent diameter (D_{ve}) and ρ_{eff} of different types of aerosol particles. This system was then used to analyze the characteristics of particles emitted from diesel vehicle engines with different mixing state (Su et al., 2021). The results showed largely different ρ_{eff} for aerosol particles emitted under launching and idling conditions (0.66 vs. 0.34 g cm⁻³). Till now, few studies have characterized the ρ_{eff} of ambient aerosol particles at different mixing state using similar tandem systems, and the evaluation of the impacts of emission controls is rare as well.

In this study, a high-resolution SPAMS coupled with a DMA and an AAC, respectively, was deployed during OWG in Beijing to characterize the chemical and physical properties of aerosol particles. The chemical composition, mixing state, and ρ_{eff} are determined, and the differences between OWG and non-Olympic Winter Games (nOWG) are explored. Particularly, the influences of emission controls on fine particle characteristics and mixing state are elucidated.

2 Methods

2.1 Sampling site and measurements

All instruments were deployed at Institute of Atmospheric Physics (IAP), Chinese Academy of Sciences ($39^{\circ}58'28''N$, $116^{\circ}22'16''E$), an urban site influenced by both residential and traffic emissions. To measure aerosol particles according to density, two tandem systems by coupling differential mobility analyzer (DMA, model 3085A, TSI Inc.) and single particle aerosol mass spectrometers (SPAMS, Hexin Analytical Instrument Co., Ltd.), aerodynamic aerosol classifier (AAC, Cambustion Ltd.) and SPAMS were operated from 21 January to 10 February, and from 10 February to 1 March, respectively (Fig. 1). Aerosol particles were first filtered with a PM_{2.5} cyclone placed in front of the sampling line. After dried with a diffusion dryer, the particles with mobility diameters (D_m) of 150, 200, 250 and 300 nm were selected by DMA, and those with aerodynamic diameter (D_a) of 300 nm were selected by AAC, and then the highly monodispersed particles were measured by SPAMS. The detailed description of AAC is given elsewhere (Liu et al., 2020; Liu et al., 2019; Yu et al., 2022). Before the campaign, the size calibration of SPAMS was performed using polystyrene latex spheres (PSLs) with known sizes (0.23, 0.32, 0.51, 0.74, 0.96, 1.4, and 2 μm).

A seven-wavelength (370, 470, 520, 590, 660, 880, and 950 nm) Aethalometer (AE33, Magee Scientific Corp.) and a high-resolution time-of-flight aerosol mass spectrometer (HR-ToF-AMS) were deployed at the same site to measure equivalent black carbon (eBC) and non-refractory organics (Org), sulfate (SO₄), nitrate (NO₃), ammonium (NH₄), and chloride (Chl) in PM₁. The time resolution of both instruments was 1 min, where HR-ToF-AMS was measured in V-mode and the mass concentration of eBC obtained by AE33 was calculated based on the dual-spot measurement (Rajesh and Ramachandran, 2018; Drinovec et al., 2015). The HR-ToF-AMS data were analyzed by using PIKA v 1.24, which showed that NO₃ (4.30 $\mu g m^{-3}$) and Org (3.80 $\mu g m^{-3}$) contributed 68.0 % of the mass concentration of non-refractory submicron aerosols (NR-PM₁, 11.92 $\mu g m^{-3}$), followed by SO₄ (1.91 $\mu g m^{-3}$), NH₄ (1.69 $\mu g m^{-3}$), and Chl (0.22 $\mu g m^{-3}$). Organic aerosols (OA) were analyzed by positive matrix factorization (PMF), and five OA factors were identified including biomass burning and fossil fuel combustion-related OA (FFBBOA), cooking OA (COA), and three SOA factors, i.e., two oxygenated OA (OOA1 and OOA2) and an aqueous-phase OOA with mass concentrations of 0.31, 0.87, 0.83, 1.18 and 0.56 $\mu g m^{-3}$, respectively. More details on the operations and data analysis of AE33 and HR-ToF-AMS are given in Xu et al. (in preparation).

2.2 Data analysis

2.2.1 SPAMS

A total of 2619,193 particles were sized and approximately 760,000 particles with both mass spectra and size information were captured by SPAMS (Table S1). As shown in Fig. S1, the counts of total particles correlated reasonably well with non-

refractory submicron aerosols (NR-PM₁, $r = 0.76$), and those of EC-containing particles correlated well with eBC ($r = 0.87$). The data were then analyzed using a neural network algorithm based on adaptive resonance theory (ART-2a) (Song et al., 1999). The vigilance factor, learning rate and iterations for ART-2a were set as 0.75, 0.05 and 20, respectively in this study. 105 According to the mass spectral characteristics, temporal trends and size distributions (Dall'osto and Harrison, 2006; Phares et al., 2001), more than 99 % of the total particles were grouped into seven major classes including Total-EC, Total-ECOC, Total-OC, Total-IA, Biomass-K, HOM and Metals, and several subclasses (Table 1). The classification of particles is based on three principles: (1) particles with distinct C_n^\pm ($n = 1, 2, 3\dots$) signals are named as EC; (2) particles with distinct OC signals (including $27[C_2H_3]^+$, $37[C_3H]^+$, $43[C_2H_3O]^+$, $50[C_4H_2]^+$, $51[C_4H_3]^+$...) are named as OC; and (3) particles are named 110 as ECOC when having comparable EC and OC signals in the positive spectra (Sun et al., 2022a; Sun et al., 2022b). The detailed names of particle types and characteristics are given in Table S2, and the average mass spectra of each type of particle are depicted in Figs. 2 and S2.

2.3.2 Effective density

Given that DMA and AAC are selected for mobility diameter (D_m) and aerodynamic diameter (D_a) of particles, respectively, 115 two methods are adopted to calculate the ρ_{eff} in this study. For the DMA-SPAMS tandem system, the ρ_{eff} is determined as the ratio of vacuum aerodynamic diameter (D_{va}) to D_m as Eq. (1).

$$\rho_{eff} = \frac{D_{va}}{D_m} \rho_0 \quad (1)$$

Where ρ_0 is the standard density (1.0 g cm⁻³).

For the AAC-SPAMS tandem system, the ρ_{eff} is calculated as the ratio of particle density (ρ_p) and particle dynamic shape 120 factor (χ_y):

$$\rho_{eff} = \frac{\rho_p}{\chi_y} = \frac{D_{va}}{D_{ve}\rho_0} \quad (2)$$

where D_{ve} represents the volume equivalent diameter. A more detailed description of the relationship between D_a , D_{va} and D_{ve} is given in Decarlo et al. (2004). Combining the calculated ρ_{eff} with the particle mixing states measured by SPAMS makes it possible to analyze the ρ_{eff} of particles with different compositions.

125 3 Results and discussion

3.1 Mixing state of aerosol particles

Figure 3 depicts the time series of meteorological parameters, pollutant concentrations and the number fractions of seven types of particles during the entire study. The average ($\pm 1\sigma$) mass concentrations of NR-PM₁ and eBC for the entire study 130 were $11.92 (\pm 15.77)$ and $1.34 (\pm 1.41)$ $\mu\text{g m}^{-3}$, respectively, and they decreased by 48.7 % and 37.5 % during OWG compared with the nOWG period (Table 2). In addition to emission controls, the favorable meteorological conditions during OWG as indicated by lower RH and T , and higher WS also played a role for the low concentrations (Liu et al., 2022).

Figure S3 shows the digital mass spectra of all particles for the whole period. Significant ion peaks of organic and carbon clusters in positive spectra, and nitrate ($46[\text{NO}_2]^-$ and $62[\text{NO}_3]^-$) and sulfate ($97[\text{HSO}_4]^-$) in negative spectra were observed. This was consistent with the AMS measurements that nitrate and organics were the major components of NR-PM₁, on average 135 accounting for 36.1 % and 31.9 %, respectively, followed by sulfate (16.0 %). The differences in the relative peak areas of aerosol particles between OWG and nOWG periods were also observed (Fig. S3b). The signals of $39[\text{K}]^+$ and organic carbon ($27[\text{C}_2\text{H}_3]^+$, $43[\text{C}_2\text{H}_3\text{O}]^+$, $50[\text{C}_4\text{H}_2]^+$) and $97[\text{HSO}_4]^-$ were significantly enhanced during OWG, suggesting the increased 140 importance of organic aerosol and sulfate. In addition, we found that the ratio of peak area of sulfate to nitrate ($\text{PA}_{\text{sulfate}}/\text{PA}_{\text{nitrate}}$) during OWG (0.26) was slightly higher than that during nOWG (0.24), suggesting the elevated aging of aerosol particles. In fact, the daily captured particle counts from SPAMS show that aging particles become more prominent during the OWG period due to the combination of the significant reduction in the number concentration of primary particles (e.g., Total-EC decreased by 61.80%) and the marked increase in the number concentration of some aging particles, such as ECOC-NS (17.34% increase), during the OWG period (Table S3).

The Total-ECOC particles with intense ion peaks of elemental carbon (EC, C_n^\pm , $n = 1, 2, 3\dots$) and organic carbon (OC, 145 $27[\text{C}_2\text{H}_3]^+$, $37[\text{C}_3\text{H}]^+$, $43[\text{C}_2\text{H}_3\text{O}]^+$, $50[\text{C}_4\text{H}_2]^+$, $51[\text{C}_4\text{H}_3]^+$) represented 47.1 % of the total particles, followed by Total-EC (13.4 %) and Biomass-K (13.0 %). The carbonaceous particles accounting for 71.0 % of the total were divided into 12 150 subclasses (Table 1). These carbonaceous particles were overall mixed with nitrate (relative peak area ~ 0.4) or sulfate ($\sim 0.05\text{--}0.2$), and showed pronounced $39[\text{K}]^+$, $23[\text{Na}]^+$ or $18[\text{NH}_4]^+$ signals in the positive spectra. We observed a clear decrease in Total-EC from 11.5 % to 8.5 % during OWG, while increased contributions for Total-ECOC and Biomass-K by 3.3 and 2.2 %, respectively. These results indicate the changes of mixing state of aerosol particles during OWG. Most 155 importantly, the composition of carbonaceous particles also changed significantly. The largest decreases were observed for EC-NS and KEC-N by 5.5 and 3.4 %, respectively, while the proportion of ECOC-NS increased significantly from 16.8 % to 28.4 %. In addition, the ammonium-containing ($18[\text{NH}_4]^+$) and trimethylamine-containing ($58[\text{C}_3\text{H}_8\text{N}]^+$ and $59[\text{C}_3\text{H}_9\text{N}]^+$) particles were largely reduced from 8.7 % to 1.1 % during OWG. Such results indicate that emission controls during OWG reduced the mixing of EC with inorganic aerosol species and amines, yet increased the mixing of EC with organic aerosol.

The Biomass-K particles were identified with intense $39[\text{K}]^+$ and levoglucosan ion peaks ($45[\text{CHO}_2]^-$, $59[\text{C}_2\text{H}_3\text{O}_2]^-$, 160 $71[\text{C}_3\text{H}_3\text{O}]^-$ and $73[\text{C}_3\text{H}_5\text{O}_2]^-$). Pratt et al. (2011) found that levoglucosan can degrade rapidly due to atmospheric oxidation. Therefore, the contribution of 13.0 % in this measurement indicated that the Biomass-K particles may undergo atmospheric 165 oxidation processes to some extent. A class of high-molecular-weight organic matter (HOM) characterized by distinct polycyclic aromatic hydrocarbons (PAHs) e.g., $152[\text{C}_{12}\text{H}_8]^+$, $165[\text{C}_{13}\text{H}_9]^+$, $178[\text{C}_{14}\text{H}_{10}]^+$, and $189[\text{C}_{15}\text{H}_9]^+$ was also detected (Zhang et al., 2022c), accounting for 5.5 % of the total particles. The prominent nitrate ($46[\text{NO}_2]^-$ and $62[\text{NO}_3]^-$) signals in negative spectra indicated the mix of HOM particles with secondary inorganic aerosol species (Fig. 2e). In addition, SPAMS also detected some relatively pure inorganic aerosol (IA) particles that did not mix with other components, and metal particles (55[Mn]⁺, 56[Fe]⁺ and 206,207,208[Pb]⁺) that were likely from anthropogenic emission and road dust. A large number of 170 rich-Fe particles with peak area ratio $56[\text{Fe}]^+/54[\text{Fe}]^+ > 3$, accounting for 59.1 % of Metals particles, were mainly observed during periods with snowfall events, and were strongly associated with secondary species especially nitrate (Fig. S2). Total-IA and Metals accounted for 7.0 % and 3.5 % of the total particles, respectively, both of which showed decreased contributions

170 during OWG, indicating the suppressed local secondary formation due to reduced precursors and the effect of stopping construction activities.

170 3.2 Diurnal cycles and sources

175 Figure 5 depicts the diurnal variations of the normalized counts of different types of particles throughout the campaign. Particles including KECOC-NS and KOC-N showed similar diurnal cycles with the lowest values occurring at 16:00 and high values at night. The high correlations of these particles with primary OA from fossil fuel combustion and biomass burning ($r = 0.78$ and 0.70 , Table S4) highlight their dominant sources of primary emissions. Consistently, the dominant contribution (OWG vs. nOWG: 48.1 vs. 47.2 %) of KECOC-NS and KOC-N to the carbonaceous particles at low PA_{sulfate}/PA_{nitrate} (< 0.2), an indicator of particle aging level (Li et al., 2020), supported the properties of fresh emissions as well (Fig. 6). The bivariate polar plots (Fig. S4) indicated that these two types of particles were mainly transported from the southeast during OWG. This result suggests that fresh particles in winter in Beijing could also be from regional transport over a small scale under emission control. Previous studies have demonstrated that particles with significant organic nitrogen fragments (26[CN]⁻ and 42[CNO]⁻) and 39[K]⁺ signals may come from wildfires, biomass burning and coal combustion (Pratt et al., 2011; Zauscher et al., 2013; Hu et al., 2021b; Bi et al., 2011). Considering the strict emission controls in Beijing during OWG, the higher normalized count of KECOC-CN at night was likely attributed to the regional transport of primarily emitted particles near Beijing (Fig. S4). However, the low peak area ratio of EC to OC (PA_{EC}/PA_{OC}) for ECOC-containing particles indicated overall higher aging levels during OWG (Fig. 7e-j) (Pio et al., 2011; Pokhrel et al., 2016). Particularly, the PA_{EC}/PA_{OC} of KECOC-NS and KECOC-CN decreased obviously from 1.01 to 0.82, and 0.92 to 0.80, respectively, during OWG.

190 The pronounced diurnal cycle of HOM indicated the sources of coal combustion and traffic emissions from heavy duty vehicles and diesel trucks, and the transport from the southeast (Fig. S4), which reached a maximum weight in total particles around 8:00 (11.4 % for OWG and 10.2 % for nOWG, Fig. 4). A pronounced diurnal cycle with high values in the morning (~11:00) was also observed for ECOC-NS, likely indicating the similar sources as HOM, yet the strong 97[HSO₄]⁻ signal in mass spectra suggested more aged properties. The moderate correlation ($r = 0.63$) between ECOC-NS and HOM and the bivariate polar plots especially during nOWG (Fig. S4b) also supported this conclusion. In fact, the ECOC-NS particles are important across different PA_{sulfate}/PA_{nitrate} values demonstrating the complexity of its sources (Fig. 6b, d).

195 In addition, KNa-containing carbonaceous particles are generally considered to be from the incomplete combustion of solid fuels such as coal combustion and traffic emissions (Xie et al., 2020; Hu et al., 2021b; Li et al., 2018). KNaEC-N and KNaECOC-NS particles were mixed a considerable nitrate (Fig. S2). The high correlations with FFBBOA and chloride (Table S4), and the bivariate polar plots of the particles emphasized the features of local emissions.

200 The types of KEC-N, EC-NS, KAECOC-NS, K-Amine-NS and K-N particles were closely associated with three SOA factors (Table S4). KEC-N and EC-NS accounted for ~75.4 % of Total-EC with relatively small daily variations (Fig. 5f) and greater contribution in the afternoon, which was particularly evident during nOWG (Fig. 4d, h). This result might indicate the background or regional characteristics of these particles, which was consistent with the conclusion of Dall'osto et al.

(2016). Interestingly, the contribution of Total-EC to the total particles decreased from 15.4 % to 5.5 % as the increase of $\text{PA}_{\text{sulfate}}/\text{PA}_{\text{nitrate}}$ from 0 to 1.1 during nOWG (Fig. 6c), whereas the change of Total-EC contribution was relatively flat (from 10.3 % to 7.0 %) during OWG (Fig. 6a). This was mainly attributed to the emission control which led to a decrease in the proportion of EC-containing particles at low aging levels. The minimum daily values of both KAECOC-NS and K-N particles appeared at 8:00 and gradually increased thereafter (Fig. 5i, l). Chen et al. (2020) suggested that the increase in K-N was mainly achieved through the uptake of nitrate from daytime photochemical production. KAECOC-NS particles characterized by high ammonium ($18[\text{NH}_4]^+$) signal were mainly observed during polluted periods with snowfall. Similarly, K-Amine-NS particles characterized by trimethylamine ion fragments ($58[\text{C}_3\text{H}_8\text{N}]^+$ and $59[\text{C}_3\text{H}_9\text{N}]^+$) (Bhave et al., 2002; Sodeman et al., 2005; Angelino et al., 2001) showed rapid increases in number concentrations as the increase of RH (Zhong et al., 2022). Therefore, K-Amine-NS was most likely from the aging process of primarily emitted particles (e.g., traffic emissions) or mixing with secondary components during snowfall periods (Zhong et al., 2022; Cheng et al., 2018), while it was mainly relevant to regional transport during other periods (Angelino et al., 2001; Chen et al., 2020; Chen et al., 2019). As typical secondary particles, K-Amine-NS (135.9 % increase, Fig. 7) and KAECOC-NS (38.8 %) showed pronounced increases as the increase of $\text{PA}_{\text{sulfate}}/\text{PA}_{\text{nitrate}}$ during OWG.

Over 70 % of rich-Fe particles were captured during polluted periods with high humidity (~83 % on average) and occasional snowfall. Aerosol acidification associated with urban pollutants has been well documented to play a substantial role in increasing the solubility of Fe-containing particles (Rubasinghe et al., 2010; Baker and Croot, 2010; Hand et al., 2004; Zhang et al., 2014). Thus, rich-Fe particles were related to the mixing of Fe-containing particles from anthropogenic emissions (e.g. vehicle, coal combustion) with acidic salts under high relative humidity conditions (Zhu et al., 2022).

The diurnal variation of KNa-N particles showed a clear bimodal character with high values peaking at 12:00 and 21:00 (Fig. 5n), which was similar to that of COA. This result indicates that KNa-N particles are mainly from cooking fume exhaust and photochemical processes (See and Balasubramanian, 2008; Abdullahi et al., 2013; Ito et al., 2016). Similarly, KOC-NS exhibited distinct cooking characteristics and good correlation with COA ($r = 0.72$), suggesting the sources of diverse meat cooking emissions, especially the Chinese style cooking (He et al., 2004; Zhao et al., 2007).

3.3 Effective density of aerosol particles

The average ρ_{eff} of aerosol particles for all measured sizes was 1.20 g cm^{-3} with a higher value during OWG than nOWG ($1.26 \text{ vs. } 1.15 \text{ g cm}^{-3}$, Fig. S5a), and the ρ_{eff} varied largely for different types of particles. The highly aged KAECOC-NS particles showed the highest ρ_{eff} of 1.62 g cm^{-3} (Fig. 10j) with abrupt increase in particle counts during snowfall and high RH period ($> 70 \text{ %}$, Fig. 8b), while the average ρ_{eff} of pure-EC and HOM associated with fresh primary emissions were 0.36 and 0.87 g cm^{-3} , respectively. Where the low ρ_{eff} of HOM particles associated with traffic and coal combustion and containing fragments of PAHs is also attributed to their loose structure. As shown in Fig. S5, the ρ_{eff} was characterized by a clear Gaussian distribution with the peak located at 1.3 g cm^{-3} . The ρ_{eff} was proportional to ambient particle size ($r^2 = 0.93$, Fig. S5b), which was distinct from that of fresh vehicle emissions studied by Su et al. (2021). In addition, it was found by comparing the ρ_{eff} of particles in different periods that the majority of particles have higher ρ_{eff} during the OWG period, with the most pronounced changes in EC-NS (OWG vs. nOWG: $1.10 \text{ vs. } 0.99 \text{ g cm}^{-3}$) and ECOC-NS ($1.22 \text{ vs. } 1.15 \text{ g cm}^{-3}$) (Fig. S6). The

average ρ_{eff} of fresh and fractal-structured pure-EC particles was the same (0.36 g cm^{-3}) at different periods. The ρ_{eff} of the primary emitted KECOC-NS ($1.31 \text{ vs. } 1.30 \text{ g cm}^{-3}$) and KOC-N ($1.03 \text{ vs. } 1.00 \text{ g cm}^{-3}$), which are closely related to the FFBBOA (Table S4) and have similar daily trends, do not change significantly between the two periods either. Irregular primary particles with low densities mix with other compositions into more compact spherical structures after being emitted into the atmosphere (Liu et al., 2019; Hu et al., 2021a).

We further analyzed the distribution of Total-EC and Total-ECOC particles as a function of ρ_{eff} which contributed 56.4 % and 59.1 % at low and high ρ_{eff} respectively (Fig. 9a). All EC classes except pure-EC showed bimodal distribution characteristics (Fig. 9c), including porous aggregates with low ρ_{eff} peaking at 0.8 g cm^{-3} and dense particles with higher ρ_{eff} peaking at 1.4 g cm^{-3} . The results are consistent with the conclusions of previous studies (Rissler et al., 2014; Liu et al., 2019; Ma et al., 2020; Hu et al., 2022). The low ρ_{eff} of pure-EC (0.36 g cm^{-3} on average) suggested the presence of fresh irregularly shaped EC particles from fuel combustion. For instance, the ρ_{eff} was comparable to that of diesel exhaust particles (0.25 g cm^{-3} , Qiu et al. (2014), fresh soot particles (0.39 g cm^{-3} , Rissler et al. (2014)), and propane flame particles (0.18 g cm^{-3} , Xue et al. (2009))). We also observed a considerable fraction of KNaECOC-NS (11.6 %) at low ρ_{eff} ($< 0.2 \text{ g cm}^{-3}$), indicating the major sources 250 of solid fuel combustion. Comparably, ECOC-NS and KECOC-NS dominated the total carbonaceous particles (61.7 %) during periods with high ρ_{eff} ($> 1 \text{ g cm}^{-3}$).

The temporal variations of ρ_{eff} are substantial due to the changes in chemical composition and particle mixing state, but overall in the range of $0.7\text{--}1.7 \text{ g cm}^{-3}$ for 77 % particles. As shown in Fig. 10a-e, the ρ_{eff} of most particles was relatively stable throughout the day with slightly higher values at $\sim 16:00$. Pure-EC was significantly different from the other particles with the ρ_{eff} of only 0.27 g cm^{-3} at $10:00$. This was attributed to the large amount of fresh elemental carbon particles during the morning rush hours. HOM, another class of particles related to fossil fuel combustion showed overall low ρ_{eff} ($\sim 0.90 \text{ g cm}^{-3}$), yet with a clear increase during daytime.

The PM dependence of ρ_{eff} is shown in Fig. 10. It is clear that the ρ_{eff} of almost all types of aerosol particles increased as a function of PM levels. For example, the average ρ_{eff} of Total-EC increased from 1.01 g cm^{-3} during clean periods ($\text{NR-PM}_1 < 10 \text{ } \mu\text{g m}^{-3}$) to 1.28 g cm^{-3} during polluted periods ($\text{NR-PM}_1 > 50 \text{ } \mu\text{g m}^{-3}$), indicating the formation process of pollution also led to the changes in both aerosol composition and particle density. Carbonaceous particles contributed up to 79.8 % of the total particles during the polluted period (Fig. 8e), with the most abundant EC-NS and KECOC-NS particles having an average density of 1.18 and 1.70 g cm^{-3} ($\text{NR-PM}_1 > 50 \text{ } \mu\text{g m}^{-3}$), respectively. The changes of ρ_{eff} as a function of RH were similar considering that severe pollution in winter was generally associated with high RH. We noticed that the average ρ_{eff} 260 was minimal during periods with $\text{RH} = 40\text{--}50 \text{ \%}$, which was 1.09 g cm^{-3} , coincident with the period with NR-PM_1 in the range of $20\text{--}30 \text{ } \mu\text{g m}^{-3}$. The proportion of primary OA in total OA in this case was considerable (47.7 % and 40.0 %, Fig. 8d, h), indicating that the appearance of low ρ_{eff} was mainly caused by fresh particles at moderate RH and PM concentration. The high ρ_{eff} (1.36 g cm^{-3}) corresponding to RH above 70 % was mainly associated with the pollution during the snowfall and the formation of secondary OA, which accounted for 85.5 % of OA (Fig. 8d). Particularly, the ρ_{eff} of K-Amine-NS increased by 265 more than 30 % as the increase of RH, highlighting the formation of N-containing particles through aqueous-phase processing and the change of particle density as well (Zhong et al., 2022).

4 Conclusions

This study provides a detailed analysis of chemical composition, mixing state, and effective density of ambient aerosol particles during Olympic Winter Games in Beijing by using a DMA/AAC+HR-SPAMS tandem system. Nearly 760,000 particles were classified into seven major classes including Total-EC (13.4 %), Total-ECOC (47.1 %), Total-OC (10.5 %), Total-IA (7.0 %), Biomass-K (13.0 %), HOM (5.5 %), and Metals (3.5 %). 71.0 % of particles were found to be carbonaceous particles mixed primarily with sulfate and nitrate. The emission controls during OWG led to decreases in the types of Total-EC particles from 11.5 % to 8.5 %, yet increases in aged and regional particles, e.g., ECOC-NS. The average effective density of aerosol particles between 150 and 300 nm was 1.20 g cm^{-3} , with higher values during OWG (1.26 g cm^{-3} vs. 1.15 g cm^{-3} for nOWG). The Total-EC particles dominated the total particles at low effective densities (56.4 %), and the effective densities of EC class particles except pure-EC showed a bimodal distribution peaking at 0.8 and 1.4 g cm^{-3} , respectively. Comparatively, the fresh pure-EC showed much lower density with an average effective density of 0.36 g cm^{-3} . The effective density varies largely depending on the particle types, secondary formation, and the changes in RH. Overall, high effective densities usually occur during the periods with high PM (NR-PM₁ $> 50 \mu\text{g m}^{-3}$) and RH ($> 70 \%$), highlighting the impact of aging processes on the effective density of aerosol particles. It is worth mentioning that due to the different sensitivities of the ionizing laser of SPAMS for the detection of different chemical compositions, its capability of quantitative analysis needs to be further evaluated in future studies.

Data availability. The data in this study are available from the authors upon request (sunyele@mail.iap.ac.cn).

Author contributions. YS and AD designed the research. AD, HL, WX, YZ, JS, YL and WZ conducted the measurements and experiments. AD, WX, HL, YZ and WZ analyzed the data. LL, XD, XP and ZW reviewed and commented on the paper. AD, YS and JS wrote the paper.

Competing interests. The contact author has declared that none of the authors has any competing interests.

Acknowledgements. This work was supported by the National Natural Science Foundation of China (92044301).

295

References

Abdullahi, K. L., Delgado-Saborit, J. M., and Harrison, R. M.: Emissions and indoor concentrations of particulate matter and its specific chemical components from cooking: A review, *Atmos. Environ.*, 71, 260-294, doi:10.1016/j.atmosenv.2013.01.061, 2013.

300 Anderson, T. L., Charlson, R. J., Schwartz, S. E., Knutti, R., Boucher, O., Rodhe, H., and Heintzenberg, J.: Climate forcing by aerosols: a hazy picture, *Science*, 300, 1103–1104, doi:10.1126/science.1084777, 2003.

Angelino, S., Suess, D. T., and Prather, K. A.: Formation of Aerosol Particles from Reactions of Secondary and Tertiary Alkylamines: Characterization by Aerosol Time-of-Flight Mass Spectrometry, *Environ. Sci. Technol.*, 35, 3130-3138,

305 Baker, A. R. and Croot, P. L.: Atmospheric and marine controls on aerosol iron solubility in seawater, *Mar. Chem.*, 120, 4-13, doi:10.1016/j.marchem.2008.09.003, 2010.

Bhave, P. V., Allen, J. O., Morrical, B. D., Fergenson, D. P., Cass, G. R., and Prather, K. A.: A Field-Based Approach for Determining ATOFMS Instrument Sensitivities to Ammonium and Nitrate, *Environ. Sci. Technol.*, 36, 4868-4879, doi:10.1021/es015823i 2002.

310 Bi, X., Zhang, G., Li, L., Wang, X., Li, M., Sheng, G., Fu, J., and Zhou, Z.: Mixing state of biomass burning particles by single particle aerosol mass spectrometer in the urban area of PRD, China, *Atmos. Environ.*, 45, 3447-3453, doi:10.1016/j.atmosenv.2011.03.034, 2011.

Buseck, P. R. and Posfai, M.: Airborne minerals and related aerosol particles: effects on climate and the environment, *Proc. Natl. Acad. Sci. U.S.A.*, 96, 3372-3379, doi:10.1073/pnas.96.7.3372, 1999.

315 Chang, Y., Du, T., Song, X., Wang, W., Tian, P., Guan, X., Zhang, N., Wang, M., Guo, Y., Shi, J., and Zhang, L.: Changes in physical and chemical properties of urban atmospheric aerosols and ozone during the COVID-19 lockdown in a semi-arid region, *Atmos. Environ.*, 287, 119270, doi:10.1016/j.atmosenv.2022.119270, 2022.

320 Charron, A., Harrison, R. M., and Quincey, P.: What are the sources and conditions responsible for exceedences of the 24h PM10 limit value (50 $\mu\text{ gm}^{-3}$) at a heavily trafficked London site?, *Atmos. Environ.*, 41, 1960-1975, doi:10.1016/j.atmosenv.2006.10.041, 2007.

Chen, Y., Wenger, J. C., Yang, F., Cao, J., Huang, R., Shi, G., Zhang, S., Tian, M., and Wang, H.: Source characterization of urban particles from meat smoking activities in Chongqing, China using single particle aerosol mass spectrometry, *Environ. Pollut.*, 228, 92-101, doi:10.1016/j.envpol.2017.05.022, 2017.

325 Chen, Y., Tian, M., Huang, R.-J., Shi, G., Wang, H., Peng, C., Cao, J., Wang, Q., Zhang, S., Guo, D., Zhang, L., and Yang, F.: Characterization of urban amine-containing particles in southwestern China: seasonal variation, source, and processing, *Atmos. Chem. Phys.*, 19, 3245-3255, doi:10.5194/acp-19-3245-2019, 2019.

Chen, Y., Cai, J., Wang, Z., Peng, C., Yao, X., Tian, M., Han, Y., Shi, G., Shi, Z., Liu, Y., Yang, X., Zheng, M., Zhu, T., He, K., Zhang, Q., and Yang, F.: Simultaneous measurements of urban and rural particles in Beijing – Part 1: Chemical composition and mixing state, *Atmos. Chem. Phys.*, 20, 9231-9247, doi:10.5194/acp-20-9231-2020, 2020.

330 Cheng, C., Huang, Z., Chan, C. K., Chu, Y., Li, M., Zhang, T., Ou, Y., Chen, D., Cheng, P., Li, L., Gao, W., Huang, Z., Huang, B., Fu, Z., and Zhou, Z.: Characteristics and mixing state of amine-containing particles at a rural site in the Pearl River Delta, China, *Atmos. Chem. Phys.*, 18, 9147-9159, doi:10.5194/acp-18-9147-2018, 2018.

Cheng, J., Su, J., Cui, T., Li, X., Dong, X., Sun, F., Yang, Y., Tong, D., Zheng, Y., Li, Y., Li, J., Zhang, Q., and He, K.: Dominant role of emission reduction in PM_{2.5} air quality improvement in Beijing during 2013–2017: a model-based decomposition analysis, *Atmos. Chem. Phys.*, 19, 6125–6146, doi:10.5194/acp-19-6125-2019, 2019.

Dall'Osto, M. and Harrison, R.: Chemical characterisation of single airborne particles in Athens (Greece) by ATOFMS, *Atmos. Environ.*, 40, 7614–7631, doi:10.1016/j.atmosenv.2006.06.053, 2006.

Dall'Osto, M., Beddows, D. C. S., McGillicuddy, E. J., Esser-Gietl, J. K., Harrison, R. M., and Wenger, J. C.: On the simultaneous deployment of two single-particle mass spectrometers at an urban background and a roadside site during SAPUSS, *Atmos. Chem. Phys.*, 16, 9693–9710, doi:10.5194/acp-16-9693-2016, 2016.

DeCarlo, P. F., Slowik, J. G., Worsnop, D. R., Davidovits, P., and Jimenez, J. L.: Particle Morphology and Density Characterization by Combined Mobility and Aerodynamic Diameter Measurements. Part 1: Theory, *Aerosol Sci. Tech.*, 38, 1185–1205, doi:10.1080/027868290903907, 2004.

Drinovec, L., Močnik, G., Zotter, P., Prévôt, A. S. H., Ruckstuhl, C., Coz, E., Rupakheti, M., Sciare, J., Müller, T., Wiedensohler, A., and Hansen, A. D. A.: The "dual-spot" Aethalometer: an improved measurement of aerosol black carbon with real-time loading compensation, *Atmos. Meas. Tech.*, 8, 1965–1979, doi:10.5194/amt-8-1965-2015, 2015.

Feng, Z., Liu, Y., Zheng, F., Yan, C., Fu, P., Zhang, Y., Lian, C., Wang, W., Cai, J., Du, W., Chu, B., Wang, Y., Kangasluoma, J., Bianchi, F., Petäjä, T., and Kulmala, M.: Highly oxidized organic aerosols in Beijing: Possible contribution of aqueous-phase chemistry, *Atmos. Environ.*, 273, doi:10.1016/j.atmosenv.2022.118971, 2022.

Gao, M., Liu, Z., Wang, Y., Lu, X., Ji, D., Wang, L., Li, M., Wang, Z., Zhang, Q., and Carmichael, G. R.: Distinguishing the roles of meteorology, emission control measures, regional transport, and co-benefits of reduced aerosol feedbacks in "APEC Blue", *Atmos. Environ.*, 167, 476–486, doi:10.1016/j.atmosenv.2017.08.054, 2017.

Giorio, C., Tapparo, A., Dall'Osto, M., Beddows, D. C., Esser-Gietl, J. K., Healy, R. M., and Harrison, R. M.: Local and regional components of aerosol in a heavily trafficked street canyon in central London derived from PMF and cluster analysis of single-particle ATOFMS spectra, *Environ. Sci. Technol.*, 49, 3330–3340, doi:10.1021/es506249z, 2015.

Guo, S., Hu, M., Zamora, M. L., Peng, J., Shang, D., Zheng, J., Du, Z., Wu, Z., Shao, M., Zeng, L., Molina, M. J., and Zhang, R.: Elucidating severe urban haze formation in China, *Proc. Natl. Acad. Sci. U. S. A.*, 111, 17373–17378, doi:10.1073/pnas.1419604111, 2014.

Han, T., Xu, W., Chen, C., Liu, X., Wang, Q., Li, J., Zhao, X., Du, W., Wang, Z., and Sun, Y.: Chemical apportionment of aerosol optical properties during the Asia-Pacific Economic Cooperation summit in Beijing, China, *J. Geophys. Res.-Atmos.*, 120, 12281–12295, doi:10.1002/2015jd023918, 2015.

Hand, J. L., Mahowald, N. M., Chen, Y., Siefert, R. L., Luo, C., Subramaniam, A., and Fung, I.: Estimates of atmospheric-processed soluble iron from observations and a global mineral aerosol model: Biogeochemical implications, *J. Geophys. Res.*, 109, D17205, doi:10.1029/2004jd004574, 2004.

365 He, L., Hu, M., Huang, X., Yu, B., Zhang, Y., and Liu, D.: Measurement of emissions of fine particulate organic matter from Chinese cooking, *Atmos. Environ.*, 38, 6557-6564, doi:10.1016/j.atmosenv.2004.08.034, 2004.

Hu, D. W., Alfarra, M. R., Szpek, K., Langridge, J. M., Cotterell, M. I., Belcher, C., Rule, I., Liu, Z. X., Yu, C. J., Shao, Y. Q., Voliotis, A., Du, M., Smith, B., Smallwood, G., Lobo, P., Liu, D. T., Haywood, J. M., Coe, H., and Allan, J. D.: Physical and chemical properties of black carbon and organic matter from different combustion and photochemical sources using 370 aerodynamic aerosol classification, *Atmos. Chem. Phys.*, 21, 16161-16182, doi:10.5194/acp-21-16161-2021, 2021a.

Hu, J., Xie, C., Xu, L., Qi, X., Zhu, S., Zhu, H., Dong, J., Cheng, P., and Zhou, Z.: Direct Analysis of Soil Composition for Source Apportionment by Laser Ablation Single-Particle Aerosol Mass Spectrometry, *Environ. Sci. Technol.*, 55, 9721-9729, doi:10.1021/acs.est.0c07983, 2021b.

375 Hu, K., Liu, D. T., Tian, P., Wu, Y. Z., Li, S. Y., Zhao, D. L., Li, R. J., Sheng, J. J., Huang, M. Y., Ding, D. P., Liu, Q., Jiang, X. T., Li, Q., and Tao, J.: Identifying the Fraction of Core–Shell Black Carbon Particles in a Complex Mixture to Constrain the Absorption Enhancement by Coatings, *Environ. Sci. Technol. Lett.*, 9, 272-279, doi:10.1021/acs.estlett.2c00060, 2022.

380 Huang, R., Zhang, Y., Bozzetti, C., Ho, K., Cao, J., Han, Y., Daellenbach, K. R., Slowik, J. G., Platt, S. M., Canonaco, F., Zotter, P., Wolf, R., Pieber, S. M., Bruns, E. A., Crippa, M., Ciarelli, G., Piazzalunga, A., Schwikowski, M., Abbaszade, G., Schnelle-Kreis, J., Zimmermann, R., An, Z., Szidat, S., Baltensperger, U., El Haddad, I., and Prevot, A. S.: High secondary aerosol contribution to particulate pollution during haze events in China, *Nature*, 514, 218-222, doi:10.1038/nature13774, 2014.

Ito, K., Johnson, S., Kheirbek, I., Clougherty, J., Pezeshki, G., Ross, Z., Eisl, H., and Matte, T. D.: Intraurban Variation of Fine Particle Elemental Concentrations in New York City, *Environ. Sci. Technol.*, 50, 7517-7526, doi:10.1021/acs.est.6b00599, 2016.

385 Lei, L., Zhou, W., Chen, C., He, Y., Li, Z., Sun, J., Tang, X., Fu, P., Wang, Z., and Sun, Y.: Long-term characterization of aerosol chemistry in cold season from 2013 to 2020 in Beijing, China, *Environ. Pollut.*, 268, 115952, doi:10.1016/j.envpol.2020.115952, 2021a.

390 Lei, L., Sun, Y., Ouyang, B., Qiu, Y., Xie, C., Tang, G., Zhou, W., He, Y., Wang, Q., Cheng, X., Fu, P., and Wang, Z.: Vertical Distributions of Primary and Secondary Aerosols in Urban Boundary Layer: Insights into Sources, Chemistry, and Interaction with Meteorology, *Environ. Sci. Technol.*, 55, 4542-4552, doi:10.1021/acs.est.1c00479, 2021b.

Li, K., Ye, X., Pang, H., Lu, X., Chen, H., Wang, X., Yang, X., Chen, J., and Chen, Y.: Temporal variations in the

hygroscopicity and mixing state of black carbon aerosols in a polluted megacity area, *Atmos. Chem. Phys.*, 18, 15201-15218, doi:10.5194/acp-18-15201-2018, 2018.

395 Li, L., Li, M., Huang, Z., Gao, W., Nian, H., Fu, Z., Gao, J., Chai, F., and Zhou, Z.: Ambient particle characterization by single particle aerosol mass spectrometry in an urban area of Beijing, *Atmos. Environ.*, 94, 323-331, doi:10.1016/j.atmosenv.2014.03.048, 2014.

Li, S., Zhang, F., Jin, X., Sun, Y., Wu, H., Xie, C., Chen, L., Liu, J., Wu, T., Jiang, S., Cribb, M., and Li, Z.: Characterizing the ratio of nitrate to sulfate in ambient fine particles of urban Beijing during 2018–2019, *Atmos. Environ.*, 237, 117662, doi:10.1016/j.atmosenv.2020.117662, 2020.

400 Liu, H., Pan, X., Wu, Y., Ji, D., Tian, Y., Chen, X., and Wang, Z.: Size-resolved mixing state and optical properties of black carbon at an urban site in Beijing, *Sci. Total Environ.*, 749, 141523, doi:10.1016/j.scitotenv.2020.141523, 2020.

Liu, H., Pan, X., Wu, Y., Wang, D., Tian, Y., Liu, X., Lei, L., Sun, Y., Fu, P., and Wang, Z.: Effective densities of soot particles and their relationships with the mixing state at an urban site in the Beijing megacity in the winter of 2018, *Atmos. Chem. Phys.*, 19, 14791-14804, doi:10.5194/acp-19-14791-2019, 2019.

405 Liu, Y., Xu, X., Yang, X., He, J., Ji, D., and Wang, Y.: Significant Reduction in Fine Particulate Matter in Beijing during 2022 Beijing Winter Olympics, *Environ. Sci. Technol. Lett.*, 9, 822-828, doi:10.1021/acs.estlett.2c00532, 2022.

Ma, Y., Huang, C., Jabbour, H., Zheng, Z., Wang, Y., Jiang, Y., Zhu, W., Ge, X., Collier, S., and Zheng, J.: Mixing state and light absorption enhancement of black carbon aerosols in summertime Nanjing, China, *Atmos. Environ.*, 222, 117141, doi:10.1016/j.atmosenv.2019.117141, 2020.

410 Okuda, T., Matsuura, S., Yamaguchi, D., Umemura, T., Hanada, E., Orihara, H., Tanaka, S., He, K., Ma, Y., Cheng, Y., and Liang, L.: The impact of the pollution control measures for the 2008 Beijing Olympic Games on the chemical composition of aerosols, *Atmos. Environ.*, 45, 2789-2794, doi:10.1016/j.atmosenv.2011.01.053, 2011.

Peng, L., Li, L., Zhang, G., Du, X., Wang, X., Peng, P. a., Sheng, G., and Bi, X.: Technical note: Measurement of chemically resolved volume equivalent diameter and effective density of particles by AAC-SPAMS, *Atmos. Chem. Phys.*, 21, 5605-5613, doi:10.5194/acp-21-5605-2021, 2021.

Phares, D. J., Rhoads, K. P., Wexler, A. S., Kane, D. B., and Johnston, M. V.: Application of the ART-2a algorithm to laser ablation aerosol mass spectrometry of particle standards, *Anal. Chem.*, 73, 2338-2344, doi:10.1021/ac0015063, 2001.

420 Pio, C., Cerqueira, M., Harrison, R. M., Nunes, T., Mirante, F., Alves, C., Oliveira, C., Sanchez de la Campa, A., Artíñano, B., and Matos, M.: OC/EC ratio observations in Europe: Re-thinking the approach for apportionment between primary and secondary organic carbon, *Atmos. Environ.*, 45, 6121-6132, doi:10.1016/j.atmosenv.2011.08.045, 2011.

Pitz, M., Cyrys, J., and Karg, E.: Wiedensohler, A., Wichmann, H. E., and Heinrich, J.: Variability of apparent particle density of an urban aerosol, *Environ. Sci. Technol.*, 37, 4336–4342, doi:10.1021/es034322p 2003.

Pokhrel, R. P., Wagner, N. L., Langridge, J. M., Lack, D. A., Jayarathne, T., Stone, E. A., Stockwell, C. E., Yokelson, R. J., and Murphy, S. M.: Parameterization of single-scattering albedo (SSA) and absorption Ångström exponent (AAE) with EC / OC for aerosol emissions from biomass burning, *Atmos. Chem. Phys.*, 16, 9549-9561, doi:10.5194/acp-16-9549-2016, 2016.

Prather, K. A.: Our current understanding of the impact of aerosols on climate change, *ChemSusChem*, 2, 377-379, doi:10.1002/cssc.200900037, 2009.

Pratt, K. A., Murphy, S. M., Subramanian, R., DeMott, P. J., Kok, G. L., Campos, T., Rogers, D. C., Prenni, A. J., Heymsfield, A. J., Seinfeld, J. H., and Prather, K. A.: Flight-based chemical characterization of biomass burning aerosols within two prescribed burn smoke plumes, *Atmos. Chem. Phys.*, 11, 12549-12565, doi:10.5194/acp-11-12549-2011, 2011.

Qiu, C., Khalizov, A. F., Hogan, B., Petersen, E. L., and Zhang, R.: High sensitivity of diesel soot morphological and optical properties to combustion temperature in a shock tube, *Environ. Sci. Technol.*, 48, 6444-6452, doi:10.1021/es405589d, 2014.

Rajesh, T. A. and Ramachandran, S.: Black carbon aerosol mass concentration, absorption and single scattering albedo from single and dual spot aethalometers: Radiative implications, *J. Aerosol Sci.*, 119, 77-90, doi:10.1016/j.jaerosci.2018.02.001, 2018.

Rajesh, T. A. and Ramachandran, S.: Assessment of the coronavirus disease 2019 (COVID-19) pandemic imposed lockdown and unlock effects on black carbon aerosol, its source apportionment, and aerosol radiative forcing over an urban city in India, *Atmos. Res.*, 267, 105924, doi:10.1016/j.atmosres.2021.105924, 2022.

Ramanathan, V., Crutzen, P. J., Kiehl, J. T., and Rosenfeld, D.: Aerosols, climate, and the hydrological cycle, *Science*, 294, 2119-2124, doi:10.1126/science.1064034, 2001.

Ren, H., Kang, M., Ren, L., Zhao, Y., Pan, X., Yue, S., Li, L., Zhao, W., Wei, L., Xie, Q., Li, J., Wang, Z., Sun, Y., Kawamura, K., and Fu, P.: The organic molecular composition, diurnal variation, and stable carbon isotope ratios of PM(2.5) in Beijing during the 2014 APEC summit, *Environ. Pollut.*, 243, 919-928, doi:10.1016/j.envpol.2018.08.094, 2018.

Rissler, J., Nordin, E. Z., Eriksson, A. C., Nilsson, P. T., Frosch, M., Sporre, M. K., Wierzbicka, A., Svenningsson, B., Londahl, J., Messing, M. E., Sjogren, S., Hemmingsen, J. G., Loft, S., Pagels, J. H., and Swietlicki, E.: Effective density and mixing state of aerosol particles in a near-traffic urban environment, *Environ. Sci. Technol.*, 48, 6300-6308, doi:10.1021/es5000353, 2014.

Rubasinghe, G., Lentz, R. W., Scherer, M. M., and Grassian, V. H.: Simulated atmospheric processing of iron oxyhydroxide

450 minerals at low pH: roles of particle size and acid anion in iron dissolution, Proc. Natl. Acad. Sci. U. S. A., 107, 6628-6633, doi:10.1073/pnas.0910809107, 2010.

See, S. W. and Balasubramanian, R.: Chemical characteristics of fine particles emitted from different gas cooking methods, Atmos. Environ., 42, 8852-8862, doi:10.1016/j.atmosenv.2008.09.011, 2008.

455 Sodeman, D. A., Toner, S. M., and Prather, K. A.: Determination of Single Particle Mass Spectral Signatures from Light-Duty Vehicle Emissions, Environ. Sci. Technol. , 39, 4569-4580, doi:10.1021/es0489947 2005.

Song, X. H., Hopke, P. K., Fergenson, D. P., and Prather, K. A.: Classification of single particles analyzed by ATOFMS using an artificial neural network, ART-2A, Anal. Chem., 71, 860-865, doi:10.1021/ac9809682, 1999.

Spencer, M. T., Shields, L. G., and Prather, K. A.: Simultaneous Measurement of the Effective Density and Chemical Composition of Ambient Aerosol Particles, Environ. Sci. Technol., 41, 1303-1309, doi:10.1021/es061425+ 2007.

460 Su, B., Zhang, G., Zhuo, Z., Xie, Q., Du, X., Fu, Y., Wu, S., Huang, F., Bi, X., Li, X., Li, L., and Zhou, Z.: Different characteristics of individual particles from light-duty diesel vehicle at the launching and idling state by AAC-SPAMS, J. Hazard. Mater., 418, 126304, doi:10.1016/j.jhazmat.2021.126304, 2021.

Sun, J., Li, Y., Xu, W., Zhou, W., Du, A., Li, L., Du, X., Huang, F., Li, Z., Zhang, Z., Wang, Z., and Sun, Y.: Single-particle volatility and implications for brown carbon absorption in Beijing, China, Sci. Total Environ., 854, 158874, doi:10.1016/j.scitotenv.2022.158874, 2022a.

465 Sun, J., Sun, Y., Xie, C., Xu, W., Chen, C., Wang, Z., Li, L., Du, X., Huang, F., Li, Y., Li, Z., Pan, X., Ma, N., Xu, W., Fu, P., and Wang, Z.: The chemical composition and mixing state of BC-containing particles and the implications on light absorption enhancement, Atmos. Chem. Phys., 22, 7619-7630, doi:10.5194/acp-22-7619-2022, 2022b.

Sun, Y., Lei, L., Zhou, W., Chen, C., He, Y., Sun, J., Li, Z., Xu, W., Wang, Q., Ji, D., Fu, P., Wang, Z., and Worsnop, D. R.: A 470 chemical cocktail during the COVID-19 outbreak in Beijing, China: Insights from six-year aerosol particle composition measurements during the Chinese New Year holiday, Sci. Total Environ., 742, 140739, doi:10.1016/j.scitotenv.2020.140739, 2020.

Sun, Y., Du, W., Fu, P., Wang, Q., Li, J., Ge, X., Zhang, Q., Zhu, C., Ren, L., Xu, W., Zhao, J., Han, T., Worsnop, D. R., and Wang, Z.: Primary and secondary aerosols in Beijing in winter: sources, variations and processes, Atmos. Chem. Phys., 16, 8309-8329, doi:10.5194/acp-16-8309-2016, 2016.

475 The People's Government of Beijing Municipality: Notice of the People's Government of Beijing Municipality on Temporary Traffic Management Measures during the Beijing 2022 Winter Olympic Games and Winter Paralympic Games, http://www.beijing.gov.cn/zhengce/zfwj/zfwj2016/szfwj/202201/t20220114_2590998.html, 2022.

480 Wang, S., Zhao, M., Xing, J., Wu, Y., Zhou, Y., Lei, Y., He, K., Fu, L., and Hao, J.: Quantifying the Air Pollutants Emission Reduction during the 2008 Olympic Games in Beijing, *Environ. Sci. Technol.*, 44, 2490-2496, doi:10.1021/es9028167, 2010.

Xie, C., He, Y., Lei, L., Zhou, W., Liu, J., Wang, Q., Xu, W., Qiu, Y., Zhao, J., Sun, J., Li, L., Li, M., Zhou, Z., Fu, P., Wang, Z., and Sun, Y.: Contrasting mixing state of black carbon-containing particles in summer and winter in Beijing, *Environ. Pollut.*, 263, 114455, doi:10.1016/j.envpol.2020.114455, 2020.

485 Xu, W., Li, Z., Lambe, A. T., Li, J., Liu, T., Du, A., Zhang, Z., Zhou, W., and Sun, Y.: Secondary organic aerosol formation and aging from ambient air in an oxidation flow reactor during wintertime in Beijing, China, *Environ. Res.*, 209, 112751, doi:10.1016/j.envres.2022.112751, 2022.

Xue, H., Khalizov, A. F., Wang, L., Zheng, J., and Zhang, R.: Effects of Coating of Dicarboxylic Acids on the Mass-Mobility Relationship of Soot Particles, *Environ. Sci. Technol.*, 43, 2787-2792, doi:10.1021/es803287v 2009.

490 Yu, C. J., Liu, D. T., Hu, K., Tian, P., Wu, Y. Z., Zhao, D. L., Wu, H. H., Hu, D. W., Guo, W. B., Li, Q., Huang, M. Y., Ding, D. P., and Allan, J. D.: Aerodynamic size-resolved composition and cloud condensation nuclei properties of aerosols in a Beijing suburban region, *Atmos. Chem. Phys.*, 22, 4375-4391, doi:10.5194/acp-22-4375-2022, 2022.

Zauscher, M. D., Wang, Y., Moore, M. J., Gaston, C. J., and Prather, K. A.: Air quality impact and physicochemical aging of biomass burning aerosols during the 2007 San Diego wildfires, *Environ. Sci. Technol.*, 47, 7633-7643, doi:10.1021/es4004137, 2013.

495 Zhai, J., Lu, X., Li, L., Zhang, Q., Zhang, C., Chen, H., Yang, X., and Chen, J.: Size-resolved chemical composition, effective density, and optical properties of biomass burning particles, *Atmos. Chem. Phys.*, 17, 7481-7493, doi:10.5194/acp-17-7481-2017, 2017.

Zhang, G., Bi, X., Lou, S., Li, L., Wang, H., Wang, X., Zhou, Z., Sheng, G., Fu, J., and Chen, C.: Source and mixing state of iron-containing particles in Shanghai by individual particle analysis, *Chemosphere*, 95, 9-16, doi:10.1016/j.chemosphere.2013.04.046, 2014.

500 Zhang, J., Li, H., Chen, L., Huang, X., Zhang, W., and Zhao, R.: Particle composition, sources and evolution during the COVID-19 lockdown period in Chengdu, southwest China: Insights from single particle aerosol mass spectrometer data, *Atmos. Environ.*, 268, 118844, doi:10.1016/j.atmosenv.2021.118844, 2022a.

Zhang, J., Liu, Q., Chen, L., Li, H., Zhao, R., Huang, X., Zhang, W., and Wang, Y.: Interannual evolution of elemental carbon-containing particles in winter in the atmosphere of Chengdu, China, *Sci. Total Environ.*, 804, 150133, doi:10.1016/j.scitotenv.2021.150133, 2022b.

Zhang, J., Huang, X., Wang, Y., Luo, B., Zhang, J., Song, H., Zhang, W., Liu, P., Schäfer, K., Wang, S., Luo, J., and Wu, P.:

Characterization, mixing state, and evolution of single particles in a megacity of Sichuan Basin, southwest China, *Atmos. Res.*, 209, 179-187, doi:10.1016/j.atmosres.2018.03.014, 2018.

510 Zhang, Y., Pei, C., Zhang, J., Cheng, C., Lian, X., Chen, M., Huang, B., Fu, Z., Zhou, Z., and Li, M.: Detection of polycyclic aromatic hydrocarbons using a high performance-single particle aerosol mass spectrometer, *J. Environ. Sci.*, 124, 806-822, doi:10.1016/j.jes.2022.02.003, 2022c.

Zhao, W., Hopke, P. K., Gelfand, E. W., and Rabinovitch, N.: Use of an expanded receptor model for personal exposure analysis in schoolchildren with asthma, *Atmo. Environ.*, 41, 4084-4096, doi:10.1016/j.atmosenv.2007.01.037, 2007.

515 Zhong, Q., Cheng, C., Li, M., Yang, S., Wang, Z., Yun, L., Liu, S., Mao, L., Fu, Z., and Zhou, Z.: Insights into the different mixing states and formation processes of amine-containing single particles in Guangzhou, China, *Sci. Total. Environ.*, 846, 157440, doi:10.1016/j.scitotenv.2022.157440, 2022.

520 Zhou, R., Yan, C., Yang, Q., Niu, H., Liu, J., Xue, F., Chen, B., Zhou, T., Chen, H., Liu, J., and Jin, Y.: Characteristics of wintertime carbonaceous aerosols in two typical cities in Beijing-Tianjin-Hebei region, China: Insights from multiyear measurements, *Environ. Res.*, 216, 114469, doi:10.1016/j.envres.2022.114469, 2023.

Zhou, Y., Wu, Y., Yang, L., Fu, L., He, K., Wang, S., Hao, J., Chen, J., and Li, C.: The impact of transportation control measures on emission reductions during the 2008 Olympic Games in Beijing, China, *Atmos. Environ.*, 44, 285-293, doi:10.1016/j.atmosenv.2009.10.040, 2010.

525 Zhu, Y., Li, W., Wang, Y., Zhang, J., Liu, L., Xu, L., Xu, J., Shi, J., Shao, L., Fu, P., Zhang, D., and Shi, Z.: Sources and processes of iron aerosols in a megacity in Eastern China, *Atmos. Chem. Phys.*, 22, 2191-2202, doi:10.5194/acp-22-2191-2022, 2022.

Table 1: A summary of particle types during this campaign.

Classification of particles		Number	Percentage (%)
Total-EC	pure-EC	3317	0.45
	EC-NS	48606	6.57
	KEC-N	26250	3.33
	KNaEC-N	21076	2.85
Total-ECOC	ECOC-NS	108490	14.67
	KECOC-CN	8493	1.15
	KECOC-NS	170590	23.06
	KNaECOC-NS	35821	4.84
Total-OC	KAECOC-NS	23976	3.24
	KOC-N	38376	5.19
	KOC-NS	31240	4.22
Total-IA	K-Amine-NS	7665	1.04
	K-N	35946	4.85
Metals	KNa-N	15908	2.15
	Biomass-K	96153	13.00
High-molecular-weight organic matter (HOM)		40998	5.54
Metals	rich-Fe	15562	2.10
	other	10787	1.44

530

Table 2: Comparison of the average ($\pm\sigma$) meteorological parameters and pollutant concentrations during OWG and nOWG period.

	T (°C)	RH (%)	WS (m s ⁻¹)	NR-PM₁ ($\mu\text{g m}^{-3}$)	eBC ($\mu\text{g m}^{-3}$)
OWG	-1.2 \pm 4.4	32.0 \pm 18.1	3.6 \pm 1.6	7.8 \pm 7.4	1.0 \pm 0.8
nOWG	0.9 \pm 4.4	36.0 \pm 23.7	3.4 \pm 2.0	15.2 \pm 19.5	1.6 \pm 1.7

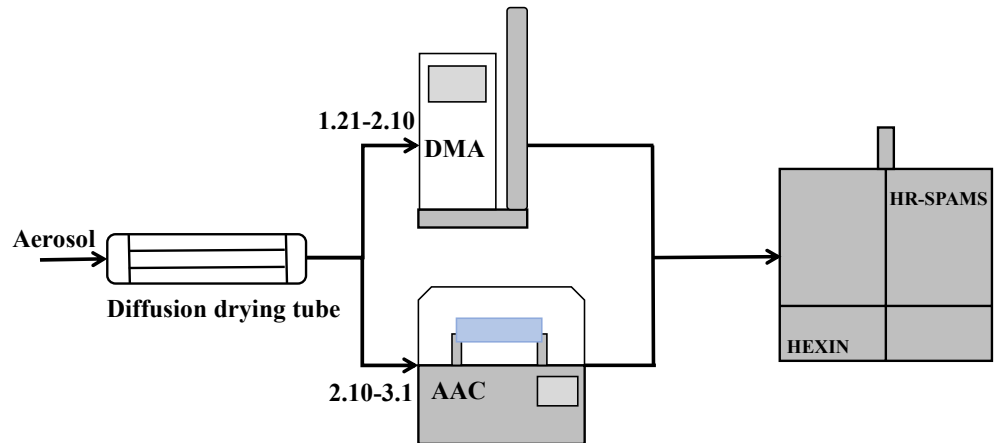


Figure 1: Schematic diagram of the experimental system.

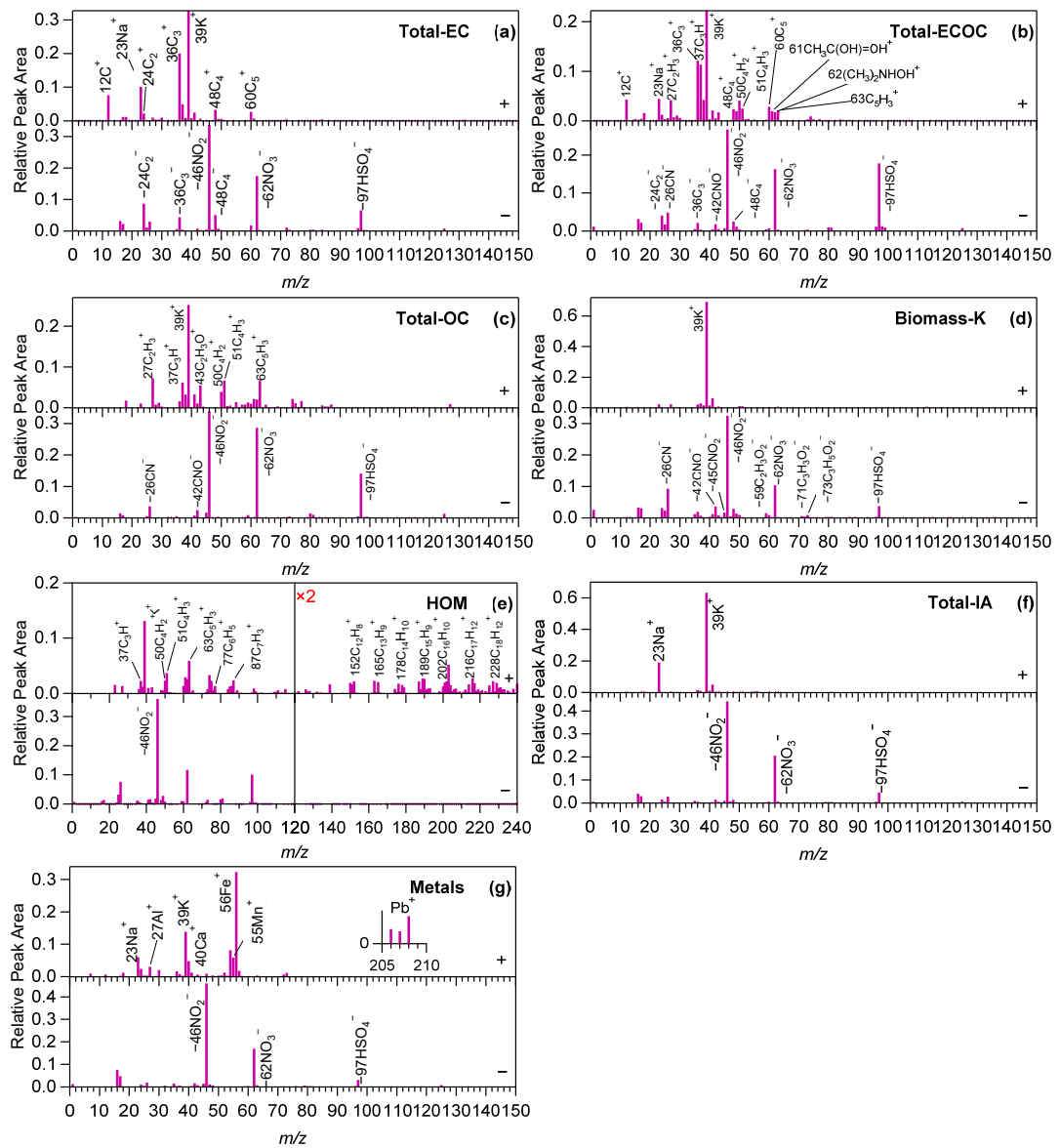
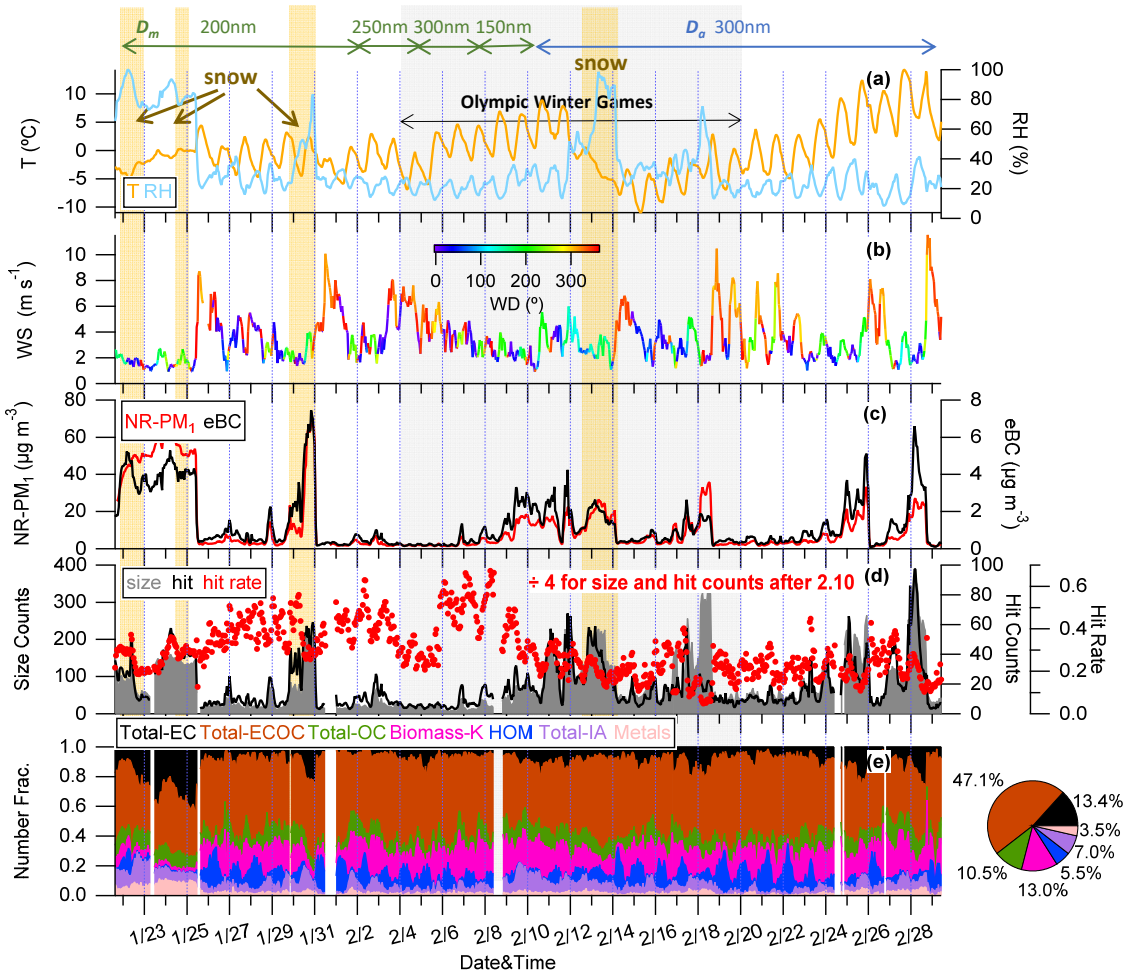


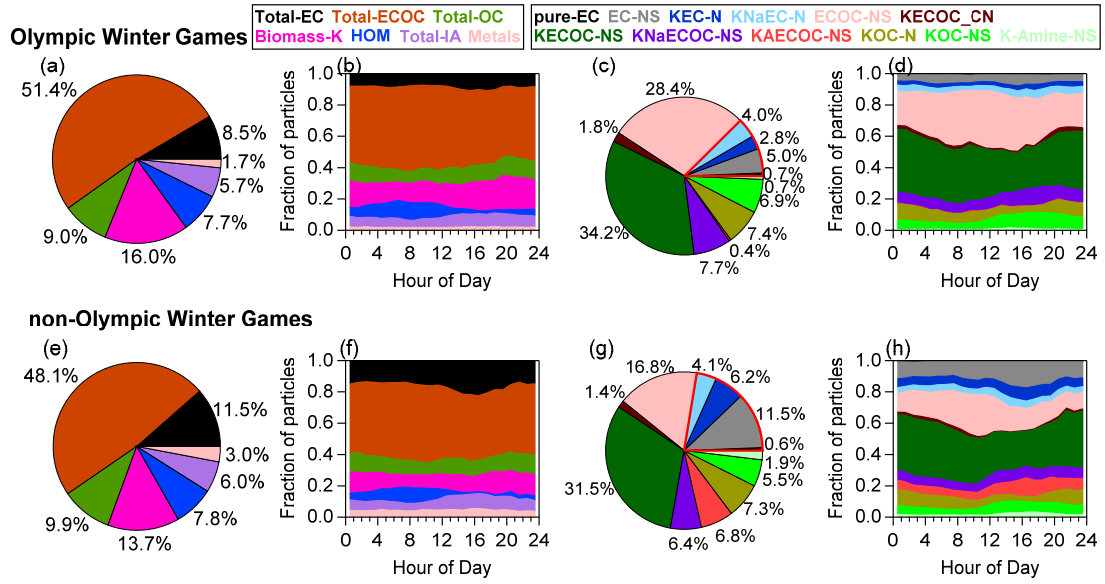
Figure 2: Average mass spectra of single particles for seven major classes.



540

545

Figure 3: Time series of (a) temperature (T) and relative humidity (RH), (b) wind speed (WS) colored by wind direction (WD, measured in degrees clockwise from due north), (c) mass concentrations of eBC and NR-PM₁, (d) number of sized particles, hit particles as well as the average hit rate of SPAMS per minute (both size and hit counts after 2.10 are divided by 4 in order to show the temporal trend of the DMA-SPAMS period better) and (e) number fraction of seven major classes of particles including Total-EC, Total-ECOC, Total-OC, Total-IA, Biomass-K, HOM and Metals. The pie chart shows the average number fraction of particles for the entire period. The green and blue arrows represent the sizes selected by DMA or AAC, respectively, while the yellow and gray shading corresponds to the snowfall and Olympic Winter Games periods, respectively.



550

Figure 4: Average contributions and diurnal fractional contributions of the major types and carbonaceous particles during (a-d) Olympic Winter Games and (e-h) non-Olympic Winter Games.

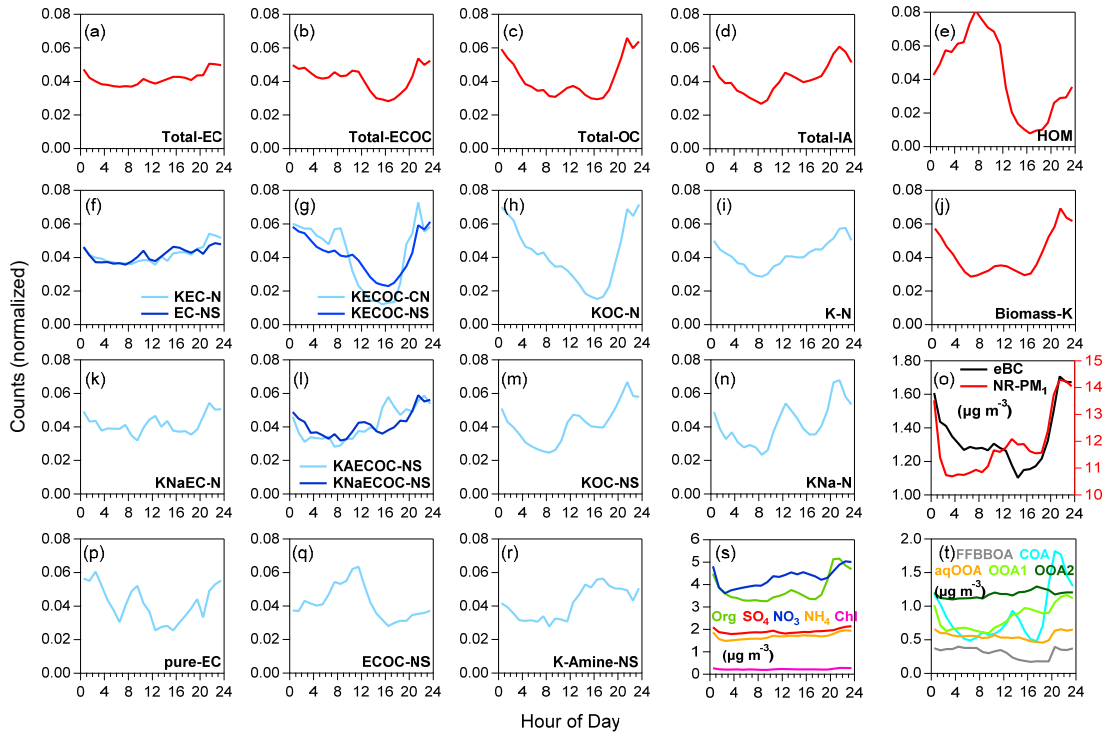


Figure 5: Diurnal cycles of (a-n, p-r) normalized counts for each class of particles, (o) mass concentrations of eBC and NR-PM₁, and (s) NR-PM₁ species, and (t) OA factors.

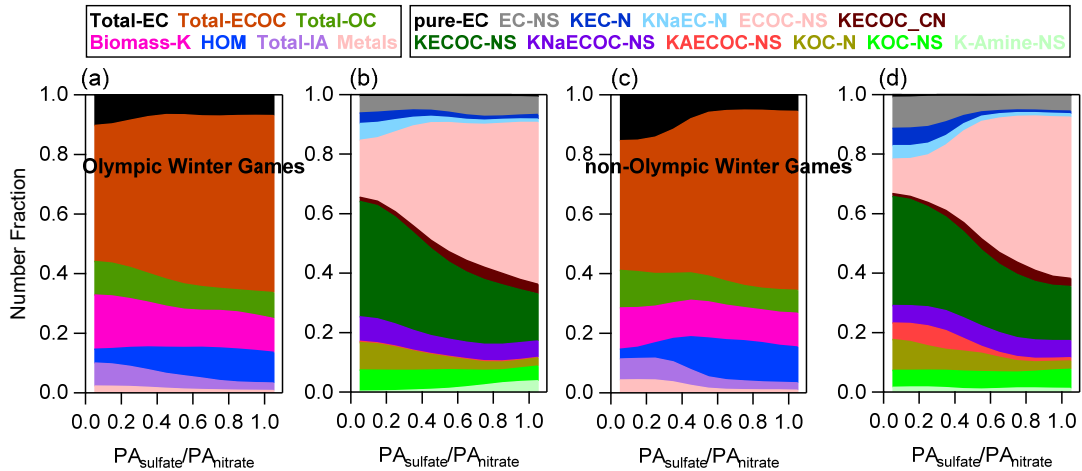


Figure 6: Variations of the average contributions of major types and carbonaceous particles as a function of peak area ratio of sulfate to nitrate during (a, b) OWG and (c, d) nOWG.

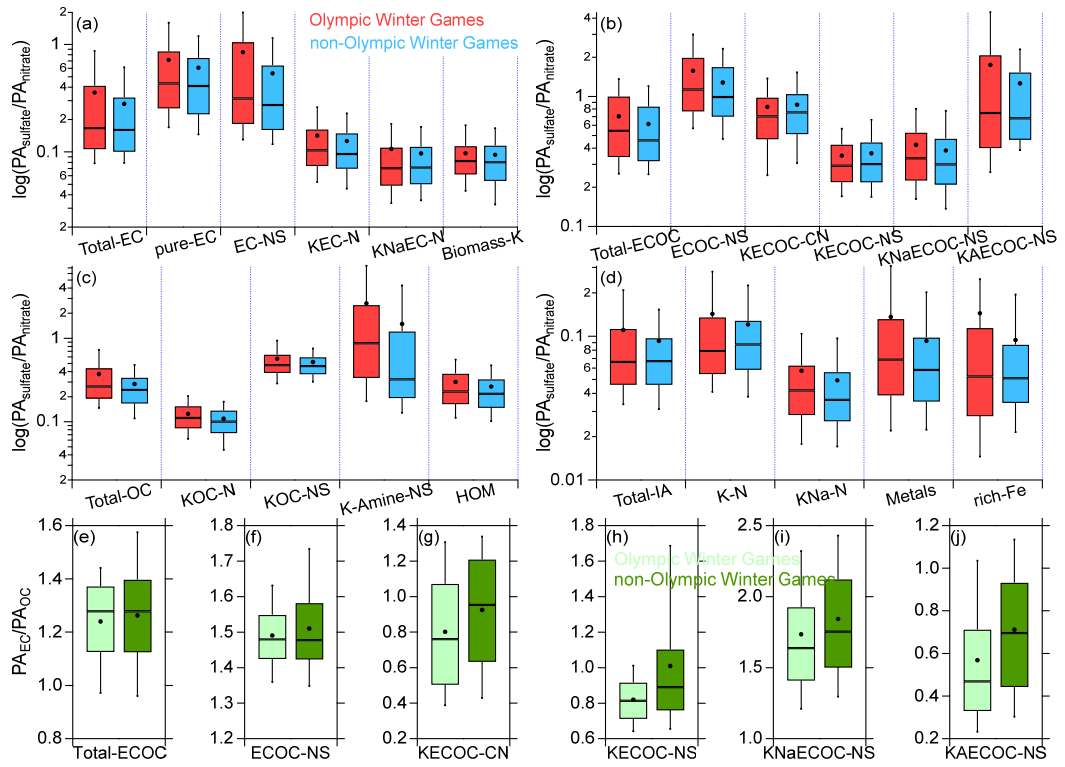


Figure 7: Peak area ratios of (a-d) sulfate (m/z 80 and 97) to nitrate (m/z 46 and 62) for each type of particles and (e-j) elemental carbon (m/z C_n^\pm , $n = 1-5$) to organic carbon (m/z 27, 29, 37 and 43) in ECOC-containing particles during O WG and nOWG. Also shown are median (horizontal lines), mean (circles), 25th and 75th percentiles (lower and upper boxes), and 10th and 90th percentiles (lower and upper whiskers).

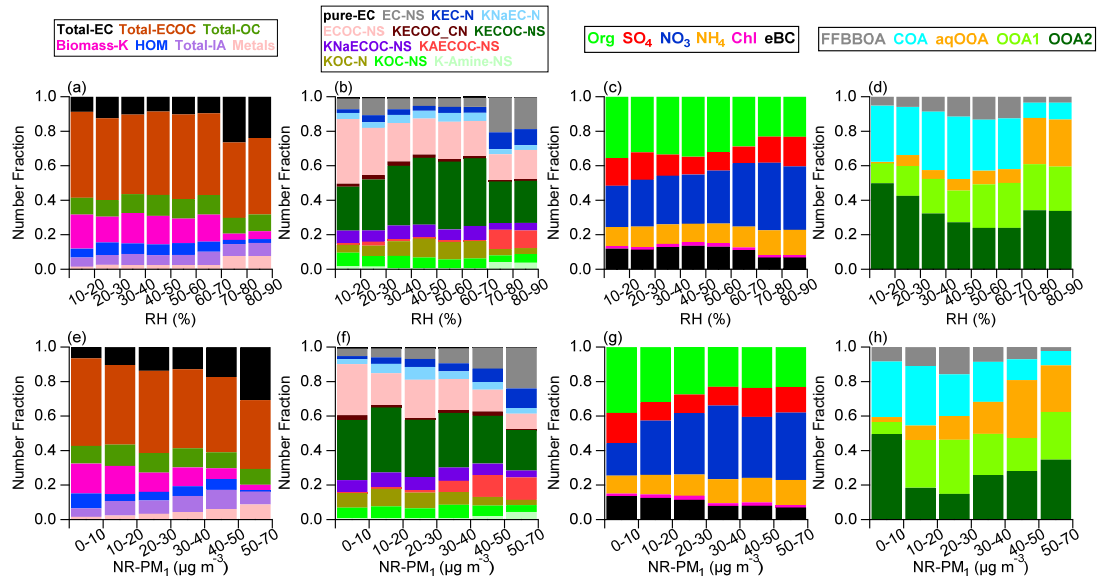
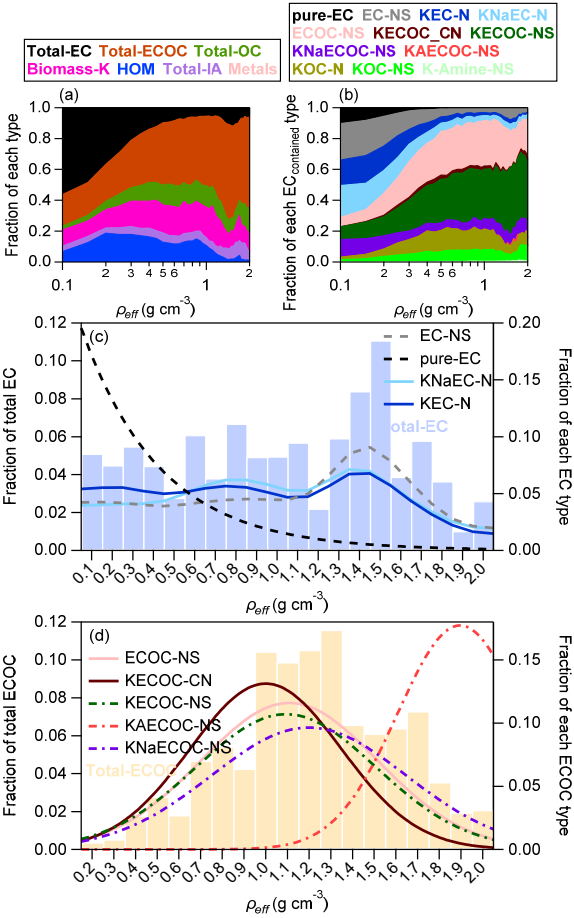


Figure 8: Variations of the number fractions and mass fractions of aerosol particles and species as a function of (a-d) relative humidity and (e-h) NR-PM₁ mass concentrations.



570

Figure 9: Average contributions of (a) major types and (b) carbonaceous particles as a function of ρ_{eff} . The distributions of ρ_{eff} for (c) Total-EC and (d) Total-ECOC particles. The left y-axis is applied to the column diagram and the right y-axis is applied to the density fitting curves.

575

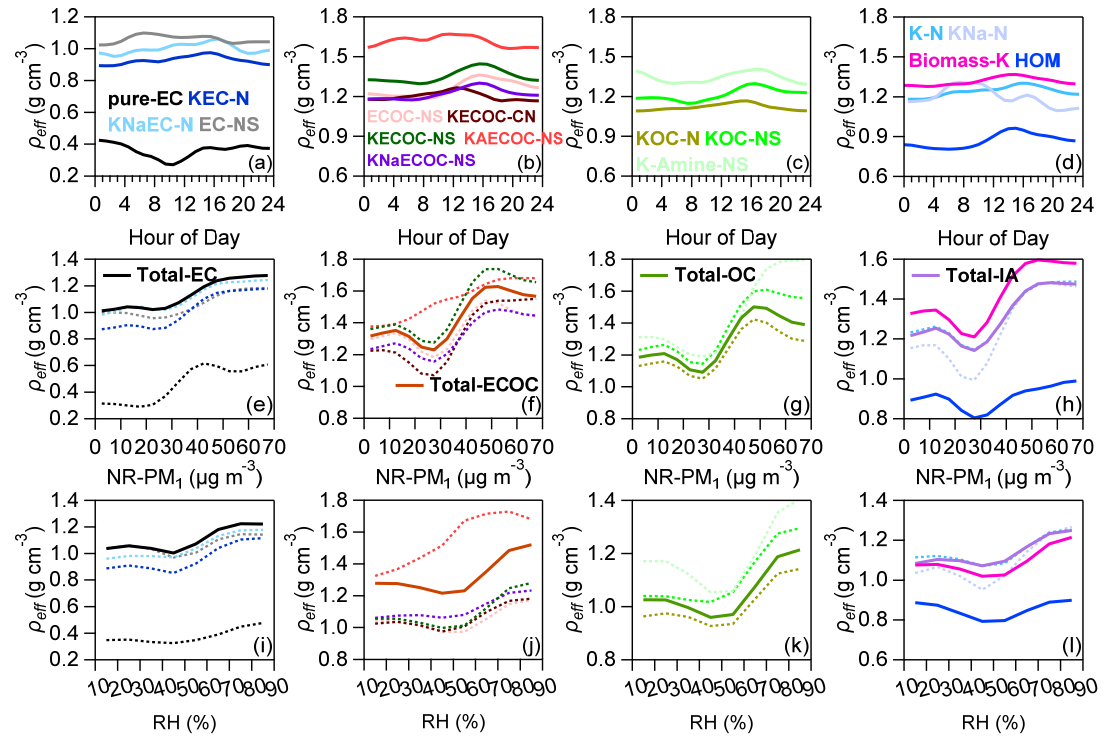


Figure 10: Diurnal variations of ρ_{eff} of each particle species (a-d). And variations of ρ_{eff} as a function of (e-h) mass concentration of NR-PM₁ and (i-l) relative humidity. Where the ρ_{eff} for each particle type is averaged over the sum of all D_m and D_a sizes.